Research

Check for updates

Indentation into a plastic fluid layer

Thomasina V. Ball[1], Neil J. Balmforth[2], and Ian J. Hewitt[3]

[1]BP Institute, Department of Earth Sciences, University of Cambridge, CB3 0EZ, U.K.
[2]Department of Mathematics, University of British Columbia, 1984 Mathematics Road, Vancouver, BC, V6T 1Z2, Canada
[3] Mathematical Institute, University of Oxford, OX2 6GG, U.K.

We study the indentation of a rigid object into a layer of a cohesive or non-cohesive plastic material. Existing approaches to this problem using slip-line theory assume that the penetration depth is relatively small, employing perturbation theory about a flat surface. Here, we use two alternative approaches to account for large penetration depths, and for the consequent spreading and uplift of the surrounding material. For a viscoplastic fluid, which reduces to an ideal plastic under the limit of vanishing viscosity, we adopt a viscoplastic version of lubrication theory. For a Mohr-Coulomb material, we adopt an extension of slip-line theory between two parallel plates to account for arbitrary indenter shapes. We compare the theoretical predictions of penetration and spreading with experiments in which a flat plate, circular cylinder or sphere are indented into layers of Carbopol or glass spheres with successively higher loads. We find reasonable agreement between theory and experiment, though with some discrepancies that are discussed. There is a clear layer-depth dependence of the indentation and uplift for the viscoplastic material. For a cylinder indented into a Mohr-Coulomb material, there is a much weaker dependence on layer depth.

THE ROYAL SOCIETY
PUBLISHING

1. Introduction

The indentation of a rigid object into the surface of a deformable plastic layer has been studied extensively in solid mechanics in the context of determining the bearing capacity of a foundation [1–3] and to provide a theoretical basis for rolling friction [4,5] and the Brinell hardness test [6]. For a layer of viscoplastic fluid, indentation is also relevant to a number of industrial coating, callendering and squeeze-flow processes [7–9], the generic washboarding instability of a towed object [10], and the migration of submerged pipelines over a muddy seafloor [11,12]. In a biological context, the formation of footprints, and the inference about the creature that made them, has been idealized as indentation into a ideal plastic layer [13–15]. In all these contexts, provided a critical load is exceeded, the insertion of the object displaces material underneath, forcing the medium to pile up around the object, adjusting the penetration depth and contact area, and thereby allowing the indenter to reach an equilibrium.

In the classical problem of the indentation of a punch into an ideal plastic, it is assumed that material begins to deform over a localized region underneath the indenter once one reaches the critical load, and the surface remains horizontal outside the region of contact. For a two-dimensional half-space indented by a flat punch, the method of characteristics, or *sliplines*, can be used to calculate the critical load exactly for a cohesive material [1] or numerically for a cohesionless medium [16]. The results can be extended to layers of finite depth [17] or nearly flat indenters of arbitrary shape [18,19]. Given the contact length a, the critical load (per unit width) is traditionally written as proportional to $a\tau_Y$ for a cohesive material with cohesion τ_Y, or $\frac{1}{2}\rho ga^2$ for a cohesionless medium with density ρ compacted by gravity g. The constants of proportionality, the "Terzaghi coefficients", account for effects such as layer confinement and indenter shape. Nevertheless, this classical-style analysis does not account for the finite deformation of the plastic layer and its uplift around the indenter. Consequently, the analysis must be extended to predict the depth to which the indenter penetrates for a given load.

When the layer is relatively shallow, an alternative approach to the problem is provided by Reynolds lubrication theory, developed for the flow of thin viscous films in fluid mechanics. The extension of this theory for yield-stress fluids has been used to compute the dynamics of viscoplastic squeeze flows [8], lubrication [20] and slumps with a free surface [21]. The theory captures dynamical evolution as well as the final limiting states, and applies to a variety of more general situations in two or three spatial dimensions [22]. Most closely related to the indentation problem is the lubrication model of Hewitt & Balmforth [20] describing the washboard patterns on a viscoplastic layer, which combines an analysis of the flow underneath a dragged, falling plate with the ploughed free-surface flow ahead. Notably, as flow speeds become arbitrarily small, one expects that viscoplasticity reduces to an ideal plastic limit. Thus, viscoplastic lubrication theory offers a means to model dynamic indentation into a plastic layer beyond the initial contact, where the surface is no longer flat and the penetration depth no longer negligible, with indenters of arbitrary geometries and for plastic substrates with rate-dependent rheology.

The goal of the current paper is therefore to investigate indentation into a shallow plastic fluid layer, exploiting a lubrication-style analysis. We begin by reviewing the classic results from slipline theory (§2), and then discuss viscoplastic lubrication theory for indentation into a shallow cohesive layer (§3). In §4, we then consider a Mohr-Coulomb material. In this case, the usual lubrication model cannot be immediately applied except in the unphysical limit of an arbitrarily small friction angle; instead, we generalize the analysis of Marshall [23], who reconsidered for a Mohr-Coulomb material Prandtl's solution of the compression of an ideal cohesive plastic between two plates [24]. To complement the theory, in §5 and §6, we perform experiments in which a cylinder or plate is pushed into a layer of either Carbopol or glass spheres. Aqueous suspensions of Carbopol (a main ingredient in many hair gels and other common commercial products) are well-characterized viscoplastic fluids that are adequately described by one of the simplest yield-stress fluid models, the Herschel-Bulkley constitutive law [25]. Indentation experiments with Carbopol are therefore expected to provide a demanding quantitative test of the
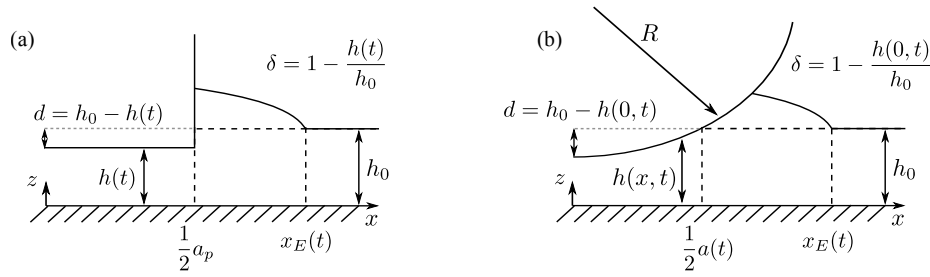
Figure 1: Sketches of the problem geometries: (a) a flat-based indenter or plate, and (b) the locally parabolic underside of a cylinder.

viscoplastic lubrication theory; the experiments with glass spheres provide a counterpart for the Mohr-Coulomb theory. We end the discussion by commenting on two other relevant issues: the effect of inertia in dynamic indentation and how a permanent impression could be imprinted on the plastic layer after the indenter is removed. Both are of particular importance in the formation of footprints, either by animal or in an industrial process.

2. Slipline theory

Following classical plasticity theory, we consider the indentation of a flat punch of length $a = a_p$ into a two-dimensional, ideal plastic layer of depth h_0, as sketched in figure 1(a). The governing equations, describing force balance and the yield condition, take the form,

$$\frac{\partial \sigma}{\partial x} + \frac{\partial \tau}{\partial z} = \frac{\partial p}{\partial x}, \qquad \frac{\partial \tau}{\partial x} - \frac{\partial \sigma}{\partial z} = \frac{\partial p}{\partial z} + \rho g \qquad \text{and} \qquad \sigma^2 + \tau^2 = (\tau_Y \cos \phi + p \sin \phi)^2, \quad (2.1)$$

where τ is the vertical shear stress, σ is the horizontal deviatoric normal stress, p is the pressure, ρ is the substrate density, g is gravity, τ_Y is the cohesion and ϕ is the friction angle. If we define

$$\sigma = (\tau_Y \cos \phi + p \sin \phi) \cos 2\vartheta \quad \text{and} \quad \tau = (\tau_Y \cos \phi + p \sin \phi) \sin 2\vartheta, \quad (2.2)$$

then the force balance equations may be manipulated into the characteristic forms,

$$\mathrm{d}z = \tan\left(\vartheta - \tfrac{1}{4}\pi - \tfrac{1}{2}\phi\right) \mathrm{d}x, \qquad \mathrm{d}p + 2(\tau_Y + p \tan \phi)\mathrm{d}\vartheta = -\rho g(\mathrm{d}z + \tan \phi \, \mathrm{d}x) \quad (2.3)$$

and

$$\mathrm{d}z = \tan\left(\vartheta + \tfrac{1}{4}\pi + \tfrac{1}{2}\phi\right) \mathrm{d}x, \qquad \mathrm{d}p - 2(\tau_Y + p \tan \phi)\mathrm{d}\vartheta = -\rho g(\mathrm{d}z - \tan \phi \, \mathrm{d}x), \quad (2.4)$$

which define the α and $\beta-$sliplines, respectively.

(a) Sliplines for a finite cohesive layer

For the case of an infinitely deep, purely cohesive layer (with $\phi = 0$), the slipline solution can be calculated analytically [1]. The slipline field consists of centred fans positioned at the edges of the indenter, opening to angles of $90°$ and buffered from one another and the free surface by right-angle triangles of constant stress; *cf.* figure 2(a) (which shows the right-half of the slipline field). This solution implies a critical load per unit width of $\tau_Y (2 + \pi)a$.

For indentation into a finite layer, following [26], we generalize this Prandtl solution using the slipline construction illustrated in figure 2. For $a < h_0\sqrt{2}$, the indenter is too narrow for the deformation to feel the bottom and the solution reduces to that of Prandtl. But if $a > h_0\sqrt{2}$, the deformation extends to the base. For that situation, we again place a centred fan and triangle of constant stress at the edge of the indenter. The construction assumes that the surfaces of both the indenter and underlying plane are rough, so that $|\tau| = \tau_Y$ along both, implying that the sliplines there have angles given by $\vartheta = \pm\tfrac{1}{4}\pi$. The centred fan can consequently be extended down to the
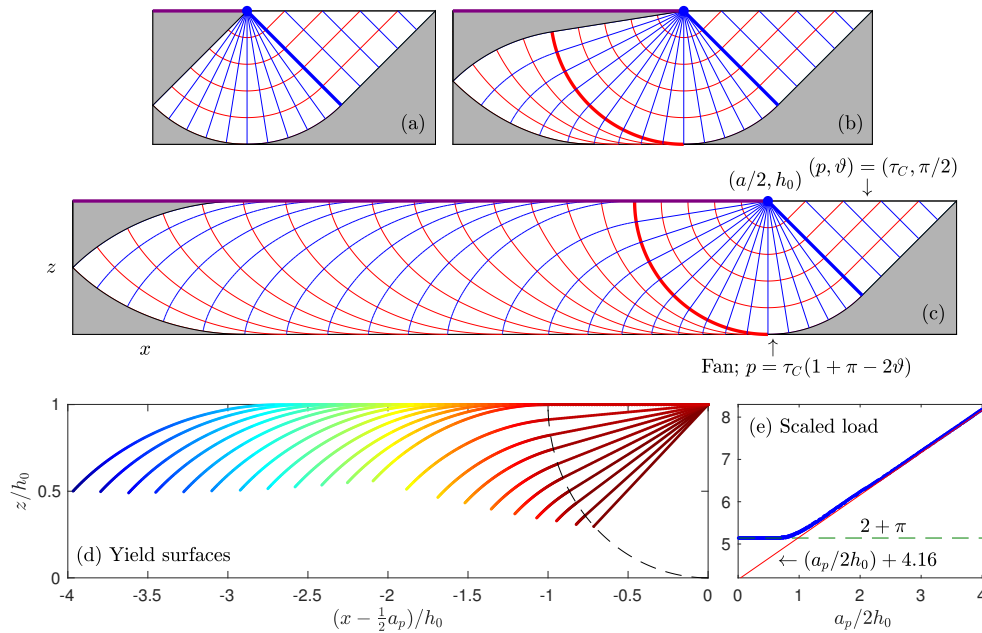
Figure 2: Sliplines for a cohesive layer, showing (a) the Prandtl solution for which the fan first touches the base ($a = \sqrt{2}h_0$), and (b)–(c) longer indenters in which the fan widens up to an angle of $3\pi/4$ and the slipline pattern is continued to the left (α−lines shown in red and β−lines in blue). The arc bounding the centred fan to the left (thicker red curve) is the α−line from which the slipline field is constructed. (d) shows a selection of upper yield surfaces for varying a_p, coloured according to the local vertical force density; the dashed line shows the edge of the fan. (e) plots the load, scaled by $aW\tau_Y$, against $\frac{1}{2}h_0^{-1}a_p$, with the shallow and deep limits indicated.

base of the layer and around towards the underside of the indenter, providing an arc along which p and ϑ are known. Further sliplines can then be launched from this arc and the bottom surface to complete the slipline field. As illustrated in figure 2(c), provided the contact length is sufficiently larger than $h_0\sqrt{2}$, the slipline pattern rapidly converges to the repeating cycloids characteristic of the squeeze flow between two plates [24]. The pattern eventually terminates underneath the centre of the indenter (assumed symmetrical about $x = 0$); here, the α and β−lines that reach $x = 0$ with angles given by $\vartheta = 0$ (as demanded by symmetry) provide yield surfaces enclosing wedges that are rigidly attached to the indenter and underlying plane.

The load for the slipline solutions is found by integrating the vertical force over the upper yield surface of the deforming region underneath the indenter (which includes part of the underside for sufficiently large a); see figure 2(d–e). As $a \to h_0\sqrt{2}$, the yielded region becomes limited to the fans and adjacent triangles of constant stress, and the load converges to $\tau_Y(2 + \pi)aW$, where W is the width of the plate. For very wide indenters, Prandtl's squeeze-flow solution gives the load $\frac{1}{2}(aW\tau_Y)(a/h_0)$. An approximation of the load for smaller contact lengths is $\frac{1}{2}(aW\tau_Y)\left(\frac{a}{h_0} + 8.32\right)$, as shown in figure 2(e). The numerically computed load switches fairly abruptly over to this approximation from the deep limit for $a \approx 2h_0$.

(b) Sliplines for a finite Mohr-Coulomb layer

For an infinitely deep non-cohesive material with $\tau_Y = 0$, the slipline field must be constructed numerically, although the pattern of sliplines superficially resembles Prandtl's solution. The
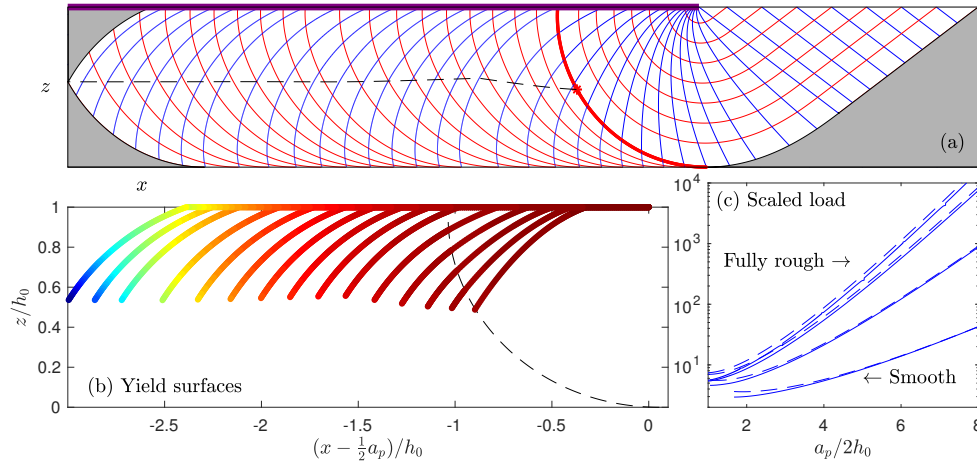
Figure 3: (a) Sliplines for a Mohr-Coulomb layer with $a = 9.2h_0$, $\phi = 24°$ and $\vartheta_f = -\frac{2}{3}(\frac{1}{4}\pi + \frac{1}{2}\phi)$. The dashed line shows the locus of the points where $\vartheta = 0$. In (b), the upper yield surfaces are shown for various a, coloured according to the local vertical force density with the overlying weight of plugged material subtracted, and with the last self-similar $\alpha-$line shown by the dashed line. In (c) we plot the load scaled by $\frac{1}{2}\rho g a^2 W$ (the Terzaghi coefficient) for $\theta_f = -[0, \frac{1}{3}, \frac{2}{3}, 1] \times (\frac{1}{4}\pi + \frac{1}{2}\phi)$. The dashed lines show the asymptotic prediction for $a \gg h_0$ in §4.

critical load per unit width is $\frac{1}{2}\rho g N_\gamma a^2$, where the Terzaghi coefficient N_γ depends on ϕ and the frictional character of the surface of the indenter [3,16].

Again, the slipline solution can be generalized to a layer of finite depth; see figure 3. In this case, the construction begins from a self-similar family of sliplines that are centred at the contact line and span a region that extends down to where the last self-similar $\alpha-$line touches the base tangentially [16,17]. The slipline field is then continued to the left by launching new sliplines from that final $\alpha-$line and the base. The boundary condition on the indenter can further be adjusted to account for surface slip by demanding that the sliplines meet the underside at a prescribed angle: $\vartheta(x, h_0) = \vartheta_f$, with $\vartheta_f = -\frac{1}{4}\pi - \frac{1}{2}\phi$ for a fully rough indenter and $\vartheta = 0$ if it is perfectly smooth; ϑ_f lies between these limits for a partially rough surface. Continuing back under the indenter, pressures now grow exponentially, negating hydrostatic contributions and allowing the slipline pattern to converge to an $x-$independent form [23], as described in more detail in §4.

3. Indentation into a shallow viscoplastic layer

(a) Viscoplastic lubrication theory

To develop a viscoplastic lubrication model of indentation, we consider a shallow layer of yield-stress fluid for which the depth is much less that the horizontal scale of the indenter, as sketched in figure 1. We use the incompressible Herschel-Bulkley model [25] to describe the fluid. Because the layer is shallow, and assuming that the fluid cannot slide freely over either the underlying plane or the indenter, the pressure p and shear stress τ play the main roles in forcing or opposing fluid motion. Ignoring the inertia of the plastic material, a standard thin-film approximation [21,22] of the force balance equations in (2.1) and mass conservation implies that

$$p_x = \tau_z \qquad p_z = -\rho g \qquad \text{and} \qquad u_x + w_z = 0, \tag{3.1}$$

where subscripts are used to indicate partial derivatives. Given the dominance of the shear stress (at least over the regions where the material is fully yielded [22,25]), the Herschel-Bulkley law

becomes one-dimensional and takes the form,

$$\tau = \left(K\dot\gamma^{n-1} + \frac{\tau_Y}{\dot\gamma} \right) u_z, \qquad \text{if } |\tau| > \tau_Y,$$

$$\dot\gamma \equiv |u_z| = 0, \qquad \text{if } |\tau| < \tau_Y, \tag{3.2}$$

where K is the consistency, n is the power-law index and τ_Y is the (constant) yield stress.

The problem splits up spatially into two pieces: below the indenter, a squeeze flow arises, with the no-slip boundary conditions on the surface demanding that

$$u(x,0,t) = w(x,0,t) = u(x,h,0) = 0 \qquad \text{and} \qquad h_t = w(x,h,t), \tag{3.3}$$

where $h(x,t)$ is the local depth of the plastic layer, which here is prescribed by the shape of the underside of the indenter. For a cylinder or plate (figure 1):

$$h(x,t) = \begin{cases} h(0,t) + \frac{1}{2}R^{-1}x^2, & \text{cylinder}, \\ h(0,t), & \text{plate}, \end{cases} \tag{3.4}$$

where R denotes the radius of curvature of the cylinder. (In appendix A, we consider axisymmetric geometry and a spherical indenter.) The squeeze flow occupies $-\frac{1}{2}a < x < \frac{1}{2}a$. Outside this interval, we ignore any ambient pressure and surface tension, and impose

$$u(x,0,t) = w(x,0,t) = 0, \qquad h_t + u(x,h,t)h_x = w(x,h,t) \qquad \text{and} \qquad p(x,h,t) = \tau(x,h,t) = 0. \tag{3.5}$$

If there is no sideways motion, the indenter falls vertically under gravity until it halts under the resistance from the substrate, which is dominated by the lubrication pressure. Given that the centre of mass lies a fixed distance above $h(0,t)$, the equation of motion of the indenter is

$$m\frac{\mathrm{d}^2}{\mathrm{d}t^2}h(0,t) = 2W\int_0^{a/2} p(x,h,t)\mathrm{d}x - mg, \tag{3.6}$$

where m and W are the indenter's mass and width.

We begin from the initial moment of contact, when $h(x,0) = h_0$ and $h_t(0,0) = \dot h_0$ (the initial layer depth and indenter speed), with $a(0) = 0$ for the cylinder and $a(0) = a(t) = a_p$ for the plate.

(b) Squeeze-flow analysis

Underneath the indenter, integrals of (3.1) indicate that

$$p(x,z,t) = P(x,t) + \rho g(h-z) \qquad \text{and} \qquad \tau(x,z,t) = \tau(x,h,t) - (P_x + \rho gh_x)(h-z), \tag{3.7}$$

where $P(x,t) = p(x,h,t)$. The constitutive law (3.2) then implies that

$$K|u_z|^{n-1}u_z + \tau_Y\,\mathrm{sgn}(u_z) = \tau(x,h,t) - (P_x + \rho gh_x)(h-z). \tag{3.8}$$

Focusing on the region $0 < x$, where $u > 0$, we observe that (3.8) and the boundary conditions $u(x,0,t) = u(x,h,0) = 0$ imply that u must be symmetric about $z = \frac{1}{2}h$. Thus,

$$u = \frac{nK^{-1/n}}{(n+1)} \times \begin{cases} (-P_x - \rho gh_x)^{1/n}[Y_-^{1+1/n} - (Y_- - z)^{1+1/n}], & 0 < z < Y_-, \\ (-P_x - \rho gh_x)^{1/n}[(h-Y_+)^{1+1/n} - (z-Y_+)^{1+1/n}], & Y_+ < z < h, \end{cases} \tag{3.9}$$

where

$$Y_\pm = \frac{h}{2} \pm \frac{\tau_Y}{|P_x + \rho gh_x|}. \tag{3.10}$$

Note that the shear stress $|\tau| < \tau_Y$ over $Y_- < z < Y_+$, implying $u_z = 0$ there. However, the horizontal flow speed,

$$u = u_p = \frac{nY_-^{1+1/n}}{(n+1)K^{1/n}}(-P_x - \rho gh_x)^{1/n}, \tag{3.11}$$

cannot be uniform in x; this region is a "pseudo-plug", where the stresses are held slightly above the yield stress, and σ has a similar magnitude to τ [22,25].

Finally, we record the depth-integrated mass-conservation equation,

$$\frac{\partial h}{\partial t} + \frac{\partial}{\partial x}\left(\int_0^h u\,\mathrm{d}z\right) = 0, \tag{3.12}$$

which (if the flow is symmetrical about $x = 0$) now implies that

$$-xh_t(0,t) = \frac{n(-P_x - \rho g h_x)^{1/n}}{(n+1)(2n+1)K^{1/n}}Y_-^{1+1/n}\left[2nh + h - 2nY_-\right], \tag{3.13}$$

and determines the surface pressure $P(x,t)$ at each instant given $h_t(0,t)$.

(c) Free-surface flow

The stress state beyond the indenter follows from the alternative boundary conditions in (3.5):

$$p = \rho g(h - z) \qquad \text{and} \qquad \tau = -\rho g h_x(h - z). \tag{3.14}$$

Hence, in view of the constitutive law and (3.5),

$$u = \frac{nK^{-1/n}}{(n+1)} \times \begin{cases} (-\rho g h_x)^{1/n}[Y^{1+1/n} - (Y-z)^{1+1/n}], & 0 < z < Y, \\ (-\rho g h_x)^{1/n}, & Y < z < h, \end{cases} \tag{3.15}$$

where

$$Y = h + \tau_Y/(\rho g h_x), \tag{3.16}$$

is a third fake yield surface underneath another pseudo-plug in $Y < z < h$. Last, we again use the mass-conservation equation (3.12), which now turns into the evolution equation,

$$\frac{\partial h}{\partial t} + \frac{\partial}{\partial x}\left[\frac{n(-\rho g h_x)^{1/n}Y^{1+1/n}(2nh + h - nY)}{(n+1)(2n+1)K^{1/n}}\right] = 0. \tag{3.17}$$

The free surface flow terminates at the flow front $x = x_E(t)$, where $h \to h_0$.

(d) Model summary

The full model problem consists of the squeeze-flow equations in $0 < x < \frac{1}{2}a$ (which amount to an ODE in x for $P(x,t)$ from (3.13), the free-surface evolution equation (3.17) for $h(x,t)$ in $\frac{1}{2}a < x < x_E$, and the equation of motion (3.6) for the indenter's elevation (which requires the pressure integral in (3.6)). The squeeze-flow and free-surface problems are coupled by the need to match the pressure and outward flux at the contact line. The former condition translates to

$$P(\tfrac{1}{2}a, t) = \rho g(h_C^+ - h_C^-) \qquad \text{and} \qquad h_C^{\pm} = h(\tfrac{1}{2}a^{\pm}, t), \tag{3.18}$$

where $x = \frac{1}{2}a^{\pm}$ denotes the limit to the contact line from underneath or outside the indenter, and $h_C^+ \neq h_C^-$ allows for a jump in depth in the case of the plate due to its vertical sides.

To place the problem in dimensionless form, we rescale time, $\tilde{t} = t\sqrt{g/h_0}$, and set

$$[\xi, \xi_C(\tilde{t}), \xi_E(\tilde{t})] = \frac{[x, \frac{1}{2}a, x_E]}{x_0}, \quad \eta(\xi, \tilde{t}) = \frac{h}{h_0}, \quad \delta(\tilde{t}) = \frac{[h_0 - h(0,t)]}{h_0}, \quad \Pi(\xi, \tilde{t}) = \frac{x_0 W P}{mg}, \tag{3.19}$$

where x_0 is the characteristic horizontal lengthscale of the indenter: for the cylinder, $x_0 \equiv \sqrt{h_0 R}$, and for the plate, $x_0 = \frac{1}{2}a_p$. In either case, we define load, gravity, and viscosity parameters,

$$\mathcal{M} = \frac{mgh_0}{\tau_Y W x_0^2}, \qquad \mathcal{G} = \frac{\rho g h_0^2}{\tau_Y x_0} \qquad \text{and} \qquad \mathcal{V} = \left(\frac{gx_0^2}{h_0^3}\right)^{1/2}\left(\frac{K}{\tau_Y}\right)^{1/n}. \tag{3.20}$$

The model system now reduces to (after dropping the hat decoration on t)

$$\mathcal{V}\xi\dot{\delta} = \frac{n|\mathcal{M}\Pi_\xi + \mathcal{G}\eta_\xi|^{1/n}}{(n+1)(2n+1)}\mathcal{Y}_-^{1+1/n}\left(2n\eta + \eta - 2n\mathcal{Y}_-\right), \quad \text{for } 0 < \xi < \xi_C^-,$$

$$\mathcal{V}\eta_t = -\frac{n\mathcal{G}^{1/n}}{(n+1)(2n+1)}\left[\mathcal{Y}^{1+1/n}(2n\eta + \eta - n\mathcal{Y})|\eta_\xi|^{1/n}\right]_\xi, \quad \text{for } \xi_C^+ < \xi < \xi_E, \tag{3.21}$$

$$\ddot{\delta} = 1 - 2\int_0^{\xi_C^-} \Pi(\xi, t)\,\mathrm{d}\xi,$$

where

$$\mathcal{Y}_\pm \equiv \tfrac{1}{2}\eta \pm |\mathcal{M}\Pi_\xi + \mathcal{G}\eta_\xi|^{-1} \quad \text{and} \quad \mathcal{Y} \equiv \eta + (\mathcal{G}\eta_\xi)^{-1}, \tag{3.22}$$

and

$$\eta(\xi, t) = \begin{cases} 1 - \delta(t) + \tfrac{1}{2}\xi^2, & \text{cylinder}, \\ 1 - \delta(t), & \text{plate}, \end{cases} \quad \text{for } 0 < \xi < \xi_C^-. \tag{3.23}$$

At the flow front, $\eta(\xi_E, t) = 1$, and at the contact line we have continuity of pressure,

$$\Pi(\xi_C^-, t) = \frac{\mathcal{G}}{\mathcal{M}}(\eta_C^+ - \eta_C^-), \tag{3.24}$$

where $\eta_C^\pm(t) = \eta(\xi, t)$ for $\xi = \xi_C^\pm$, and continuity of flux,

$$\left[\left|\frac{\mathcal{M}}{\mathcal{G}}\Pi_\xi + \eta_\xi\right|^{1/n}\mathcal{Y}_-^{1+1/n}\left(2n\eta + \eta - 2n\mathcal{Y}_-\right)\right]_{\xi=\xi_C^-} = \left[|\eta_\xi|^{1/n}\mathcal{Y}^{1+1/n}(2n\eta + \eta - n\mathcal{Y})\right]_{\xi=\xi_C^+}. \tag{3.25}$$

(e) A sample indentation

We solve (3.21)–(3.25) numerically by using centred finite differences to approximate spatial derivatives and quadrature on the same grid to evaluate the substrate resistance, then step the solution forwards in time using MATLAB's in-built solver ODE15s. Figure 4 shows a sample numerical solution for the indentation of a cylinder, displaying snapshots of the flow pattern in the viscoplastic layer, as well as time series of $\delta(t)$, $\xi_C(t)$ and $\xi_E(t)$. As the cylinder pushes into the substrate, fluid is squeezed out from underneath, building up the free surface beyond the contact line, which then collapses under gravity. The penetration of the indenter into the substrate slows and eventually stops at $t \approx 0.30$ when $\delta = \delta_f \approx 0.37$. The fluid stresses subsequently fall below the yield stress everywhere to halt all motion (the model equations hold only for $\dot{\delta} > 0$).

Note that the two flow patterns within the substrate are inconsistent at the contact line: the pseudo-plugs of the squeeze and free-surface flows do not coincide in figure 4(a–c). The discontinuity highlights the presence of a boundary layer at the contact line with a horizontal length comparable to the fluid depth. Over this region, the two flow patterns must be reconciled; in the shallow-layer theory, only the net effect is incorporated by matching the pressure and flux.

(f) Plastic limit

When $\mathcal{V} \to 0$, the resistance of the substrate is provided solely by the plastic yield stress and the flow problems are rendered quasi-static. From (3.22), we then find

$$\mathcal{M}\Pi_\xi = -\mathcal{G}\eta_\xi - \frac{2}{\eta} \text{ for } 0 < \xi < \xi_C \quad \text{and} \quad \mathcal{G}\eta\eta_\xi = -1 \text{ for } \xi_C < \xi < \xi_E, \tag{3.26}$$

which correspond to the conditions met when $(Y, Y_-) \to 0$ and $Y_+ \to h$, and the yield surfaces approach the adjacent solid walls (*cf.* figure 4(c)). Hence,

$$\mathcal{M}\ddot{\delta} - \mathcal{M} = -2\int_0^{\xi_C^-}\mathcal{M}\Pi\,\mathrm{d}\xi \equiv -2\xi_C\mathcal{G}(\eta_C^+ - \eta_C^-) + 2\int_0^{\xi_C^-}\left(\mathcal{G}\eta_\xi + \frac{2}{\eta}\right)\xi\,\mathrm{d}\xi, \tag{3.27}$$
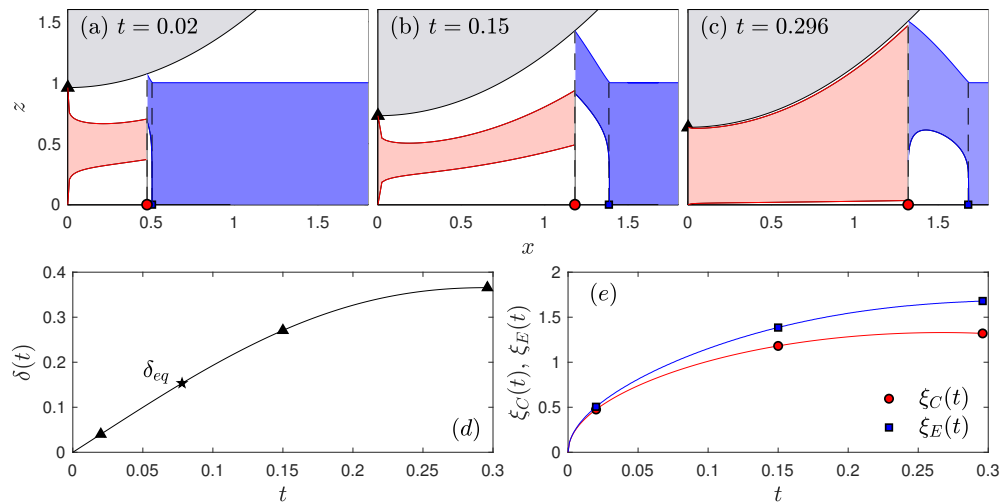
Figure 4: (a)-(c) Numerical solution for a cylinder dropped onto a Herschel Bulkley substrate with $n = \frac{1}{3}$, with $\dot{\delta}_0 = 2$ and $\mathcal{M} = \mathcal{G} = \mathcal{V} = 1$, showing three snapshots of the flow patterns. Indicated are the edge of cylinder (black), the free surface (blue), the yield surfaces in the squeeze flow (red) and free surface flow (blue); the contact line and flow front are marked by vertical dashed lines. The cylinder and plug flows are shaded. Below are time series of (d) $\delta(t)$ and (e) contact length and flow front; the triangles indicate the times of the snapshots in (a)–(e) and the star in (d) is the equilibrium depth δ_{eq} of see §3(f).

and the free surface profile and runout are

$$\eta = \sqrt{\left(\eta_C^+\right)^2 - 2\mathcal{G}^{-1}(\xi - \xi_C)} \qquad \text{and} \qquad \xi_E = \xi_C + \tfrac{1}{2}\mathcal{G}[\left(\eta_C^+\right)^2 - 1]. \tag{3.28}$$

Conservation of mass now demands that

$$\int_0^{\xi_C^-} \eta(\xi, t)\mathrm{d}\xi + \int_{\xi_C^+}^{\xi_E} \eta(\xi, t)\mathrm{d}\xi = \xi_E. \tag{3.29}$$

Below, we quote the equilibrium positions predicted by (3.27)–(3.29) when $\ddot{\delta} = 0$ for the cylinder and plate. These equilibria are not the same as the final position δ_f illustrated in figure 4, which is lower as a result of the finite inertia of the indenter. However, when the load on the indenter is slowly raised to push it incrementally into the substrate (which corresponds to raising $\mathcal{M}$ at fixed $\mathcal{G}$), as in our loading experiments, inertia is largely irrelevant and the penetration depth is set by the equilibrium position.

(i) Cylinder

For the cylinder ($\eta = 1 - \delta + \frac{1}{2}\xi^2$ for $\xi < \xi_C$, $\eta_C^+ = \eta_C^- = 1 - \delta + \frac{1}{8}a^2$, and $\Pi(\xi_C) = 0$), the equations (3.27) and (3.29) reduce to

$$\mathcal{M} = \frac{2}{3}\mathcal{G}\xi_C^3 + 4\log\left(1 + \frac{\xi_C^2}{2(1-\delta)}\right) \qquad \text{and} \qquad \xi_C^3 - \mathcal{G}(3 - 2\delta + \xi_C^2)\left(\delta - \tfrac{1}{2}\xi_C^2\right) = 6\xi_C(1 - \delta). \tag{3.30}$$

In the limit, $\mathcal{G} \ll 1$, we find $\xi_C = \sqrt{6\delta}$. For this low-gravity situation, the free surface deformation becomes localized to $\xi = \xi_C$, and a near vertical face forms at the contact line. In the opposite limit of $\mathcal{G} \gg 1$, the free surface is pulled immediately down to the height of the original layer by the

relatively strong gravity, with $\eta_C = 1$ and $\xi_C = \sqrt{2\delta}$. Note that the cylinder never makes contact with the underlying surface ($\delta \to 1$): $\delta \sim 1 - e^{-\mathcal{M}/4}$ for $\mathcal{M} \gg 1$.

(ii) Plate

For the plate ($\eta = \eta_C^- = 1 - \delta$ for $\xi < \xi_C = 1$ and $\Pi(1) = \mathcal{G}(\eta_C - 1 + \delta)$), we find

$$\mathcal{M} = 2(1-\delta)^{-1} + 2\mathcal{G}(\eta_C - 1 + \delta) \qquad \text{and} \qquad 6\delta = \mathcal{G}(\eta_C^+ - 1)^2(2\eta_C^+ + 1). \tag{3.31}$$

In this problem, the variables are δ and η_C^+, the height to which the fluid becomes piled up against the sides of the plate. Moreover, there is a threshold for penetration because of the plate's fixed length $\xi_C = 1$ (for the cylinder, $\xi_C \to 0$ as $\delta \to 0$), of $\mathcal{M} > 2$ or $\tau_Y < 2mgh_0/(Wa^2)$.

4. Indentation into a shallow Mohr-Coulomb layer

Viscoplastic lubrication theory applies when the deviatoric stresses τ and σ are much less than the pressure p, leading to scale separation and the usual simplifications of Reynolds theory. For a Mohr-Coulomb material, however, the pressure is only significantly larger than τ and σ when the friction angle of the material ϕ is unphysically small. An alternative theoretical description is then needed. For this task we return to plasticity theory, and extend the analysis of Marshall [23]. The key insight is that, when the length of indenter is much greater than the depth of the layer, the sliplines converge to a universal pattern away from the contact line.

(a) Perturbation theory

For shallow indentation, we stretch the horizontal coordinate, $X = \epsilon x$, to account for difference in spatial scales, where $\epsilon \ll 1$ corresponds to the ratio of the layer depth and the characteristic horizontal extent of the indenter (i.e. $\epsilon = h_0/x_0$ in the notation of the lubrication analysis). We then set $p = p(X, z, t)$, $\vartheta(X, z, t)$ and $h = h(X, t)$. With $\tau_Y = 0$, we have $(\sigma, \tau) = p \sin \phi (\cos 2\vartheta, \sin 2\vartheta)$, and a re-arrangement of (2.1) now gives

$$-(\log p)_z \cos^2 \phi + 2 \sin \phi \left[\vartheta_z \sin 2\vartheta + \epsilon(\cos 2\vartheta - \sin \phi)\vartheta_X \right] = \frac{\rho g}{p}(1 - \cos 2\vartheta \sin \phi), \tag{4.1}$$

$$-\epsilon(\log p)_X \cos^2 \phi + 2 \sin \phi \left[(\cos 2\vartheta + \sin \phi)\vartheta_z - \epsilon \vartheta_X \sin 2\vartheta \right] = \frac{\rho g}{p} \sin 2\vartheta \sin \phi. \tag{4.2}$$

Motivated by the exponential growth of the pressure in the squeeze flow shown by Marshall [23] and demonstrated by the slipline solutions in §2, we introduce the asymptotic sequences,

$$\log p = \frac{\sin \phi}{\cos^2 \phi} \left(\frac{F_{-1}}{\epsilon} + F_0 + \epsilon F_1 + ... \right) \quad \text{and} \quad \vartheta = \vartheta_0 + \epsilon \vartheta_1 + ... \tag{4.3}$$

The pressure rise further ensures that hydrostatic contributions become exponentially small, leading us to discard the gravity terms on the right of (4.1)–(4.2). Again, we take the bottom of the layer to be rough with $\vartheta(X, 0, t) = \frac{1}{4}\pi + \frac{1}{2}\phi$, and the indenter to be partially rough so that $\vartheta(X, h, t) \sim \vartheta_f - \epsilon h_X$, in view of the shape of the indenter.

Collecting terms of order ϵ^{-1} and ϵ^0 in (4.1)–(4.2), we now find the relations,

$$F_{-1z} = 0, \qquad F_{0z} = -(\cos 2\vartheta_0)_z \qquad \text{and} \qquad F_{-1X} = 2(\cos 2\vartheta_0 + \sin \phi)\vartheta_{0z}. \tag{4.4}$$

Hence, given that $\vartheta_0(X, 0, t) = \frac{1}{4}\pi + \frac{1}{2}\phi$ and $\vartheta_0(X, h, t) = \vartheta_f$,

$$F_{-1}(X, t) = \int_X^{A/2} \frac{C}{h(u, t)} \, du, \qquad F_0(X, z, t) = f(X, t) - \cos 2\vartheta_0 + \cos 2\vartheta_f, \tag{4.5}$$

and

$$\frac{z}{h} = \frac{\sin 2\vartheta_0 - \cos \phi + (2\vartheta_0 - \frac{1}{2}\pi - \phi)\sin \phi}{\sin 2\vartheta_f - \cos \phi + (2\vartheta_f - \frac{1}{2}\pi - \phi)\sin \phi}, \tag{4.6}$$

where $A = \epsilon a$, $f(X,t) = F_0(X,h,t)$ and

$$C = \cos\phi - \sin 2\vartheta_f - (2\vartheta_f - \tfrac{1}{2}\pi - \phi)\sin\phi. \tag{4.7}$$

The implicit solution for ϑ_0 in (4.6) reflects the convergence of the slipline pattern to a form that depends only on the rescaled vertical coordinate $z/h(X,t)$. Moreover, in (4.5) we have assumed that the solution matches to an $O(1)$ pressure at the contact line (demanding $F_{-1}(\tfrac{1}{2}A, t) = 0$).

At $O(\epsilon)$, equation (4.2) gives

$$F_{0X} = 2(\vartheta_1 \cos 2\vartheta_0 + \vartheta_1 \sin\phi)_z + (\cos 2\vartheta_0)_X, \tag{4.8}$$

which now implies that $f_X = \Upsilon(\log h)_X$, where

$$\Upsilon = 2\sin\phi - \frac{2}{C}\left[\vartheta_f - \tfrac{1}{4}\pi - \tfrac{1}{2}\phi + \sin\phi(\sin 2\vartheta_f - \cos\phi) + \tfrac{1}{4}(\sin 4\vartheta_f + \sin 2\phi)\right]. \tag{4.9}$$

Hence, to $O(1)$, the pressure is prescribed up to a dimensionless amplitude parameter Ψ (cf. [23]):

$$p = \rho g h_C \Psi \exp\left\{\frac{\sin\phi}{\cos^2\phi}\left[\frac{1}{\epsilon}\int_X^{A/2}\frac{C}{h(u,t)}\mathrm{d}u + \Upsilon\ln\left(\frac{h}{h_C}\right) - (\cos 2\vartheta_0 - \cos 2\vartheta_f)\right]\right\}. \tag{4.10}$$

(b) Matching, uplift and surface resistance

To determine Ψ, we assume that the indenter and free surface are locally flat in a narrow region around the contact line with $O(h_C)$ width. This leads us to match the pressure $p(\tfrac{1}{2}A, z, t)$ to the slipline solution of §2(b), where edge effects and gravity become important. The match provides $\Psi = \Psi(\phi, \vartheta_f)$ from the leftward limit of the slipline solution, where the sliplines converge to universal form. The local depth $h_C = h_0\eta_C$ requires a model for the free-surface uplift beyond the indenter. For a Mohr-Coulomb layer, this is problematic as the time-dependent dynamics predicted by an associated flow rule predicts an unphysical degree of dilation [27]. One path forward is to assume that the profile of the free surface is dictated by gravitational collapse to the angle of friction, in which case

$$h = h_0\eta_C - (x - \tfrac{1}{2}a)\tan\phi, \qquad \text{for } \tfrac{1}{2}a < x < \tfrac{1}{2}a + h_0(\eta_C - 1)\cot\phi. \tag{4.11}$$

Mass conservation during a quasi-static indentation then implies that

$$\int_0^{\xi_C}\eta(\xi, t)\,\mathrm{d}\xi + \tfrac{1}{2}(\eta_C - 1)^2\epsilon\cot\phi = \xi_C, \tag{4.12}$$

where, again, $\xi_C = a/(2x_0)$ and $\eta(\xi, t) = \eta(x/x_0, t) = h/h_0$. Finally, we compute the surface resistance by integrating the leading-order vertical stress $\sigma + p$ over the contact length, and feed the result into the dimensionless equation of motion of the indenter:

$$1 - \frac{2\mathcal{G}}{\mathcal{M}}\Psi(\phi, \vartheta_f)(1 + \sin\phi\cos 2\vartheta_f)\eta_C\int_0^{\xi_C}\exp\left\{\frac{\sin\phi}{\cos^2\phi}\left[\frac{1}{\epsilon}\int_\chi^{\xi_C}\frac{C\,\mathrm{d}u}{\eta(u,t)} + \Upsilon\ln\left(\frac{\eta}{\eta_C}\right)\right]\right\}\mathrm{d}\chi = \ddot{\delta}. \tag{4.13}$$

As in §3(f), we consider the equilibrium positions where $\ddot{\delta} = 0$ for different indenter shapes. The load predicted by (4.13) for a flat plate with $x = \tfrac{1}{2}a_p$ is compared with slipline computations in figure 3(c); in this instance, the slipline computation is exact, and the prediction from (4.13) corresponds to its asymptotic limit for $a_p \gg h_0$. For the cylinder (with $\eta = 1 - \delta + \tfrac{1}{2}\xi^2$),

$$\frac{\mathcal{M}}{2\mathcal{G}} = \Psi(\phi, \vartheta_f)(1 + \sin\phi\cos 2\vartheta_f)(1 - \delta + \tfrac{1}{2}\xi_C^2)\exp\left[\frac{C\sin\phi}{\epsilon\cos^2\phi}\sqrt{\frac{2}{1-\delta}}\tan^{-1}\left(\frac{\xi_C}{\sqrt{2(1-\delta)}}\right)\right] \times$$

$$\times\int_0^{\xi_C}\exp\left\{-\frac{\sin\phi}{\cos^2\phi}\left[\frac{C}{\epsilon}\sqrt{\frac{2}{1-\delta}}\tan^{-1}\left(\frac{\chi}{\sqrt{2(1-\delta)}}\right) - \Upsilon\ln\left(\frac{1 - \delta + \tfrac{1}{2}\chi^2}{1 - \delta + \tfrac{1}{2}\xi_C^2}\right)\right]\right\}\mathrm{d}\chi. \tag{4.14}$$

along with

$$\xi_C^3 + 3(\delta - \tfrac{1}{2}\xi_C^2)^2\epsilon\cot\phi = 6\xi_C\delta. \tag{4.15}$$
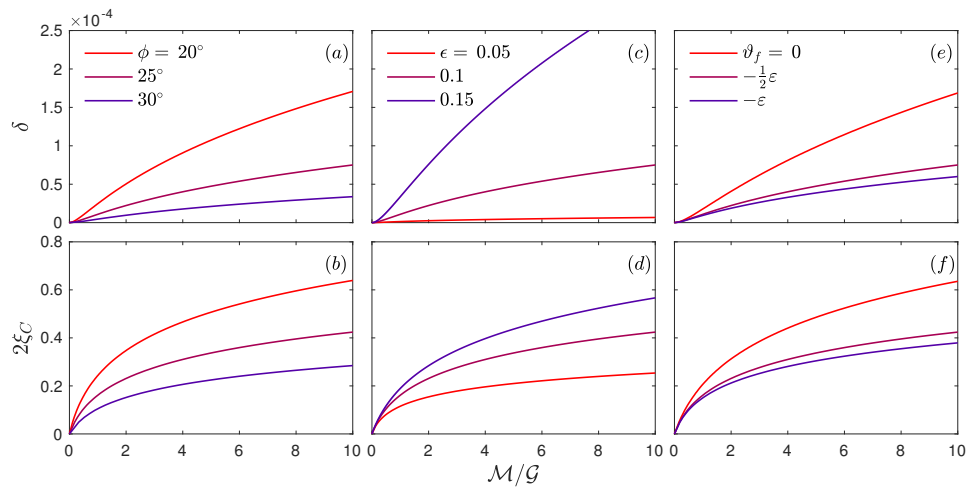
Figure 5: Penetration depth, δ, and contact length, $2\xi_C$, against non-dimensional load $\mathcal{M}/\mathcal{G}$ for (a–b) $\phi = 20,\ 25,\ 30°$, (c–d) $\epsilon = 0.05,\ 0.1,\ 0.15$, and (e–f) $\vartheta_f = -[0, \frac{1}{2}, 1] \times (\frac{1}{4}\pi + \frac{1}{2}\phi)$. Aside from those choices, the parameters are $\epsilon = 0.1$, $\vartheta_f = -\frac{1}{2}(\frac{1}{4}\pi + \frac{1}{2}\phi)$ and $\phi = 25°$.
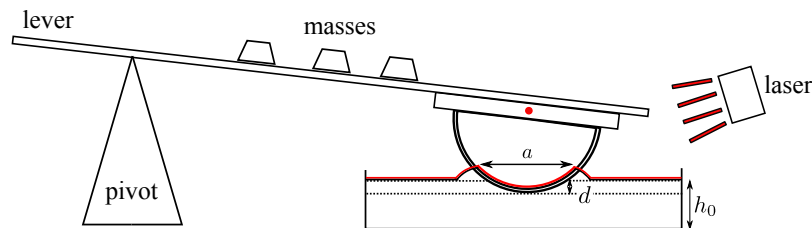

Figure 6: Sketch of the experimental set-up.

Figure 5 shows the solutions to (4.14–4.15) for different values of the friction angle ϕ, aspect ratio ϵ (equivalently, the layer thickness for a given cylinder) and cylinder roughness ϑ_f.

5. Indentation experiments with Carbopol

(a) Set-up

The setup for our indentation experiments is sketched in figure 6: an indenter was attached to the end of an aluminium bar and positioned above a tray filled with Carbopol. The metre-long bar was fixed to bearings that could rotate relatively freely about an axle. The indenter was counterbalanced so that it rested at a height just above the Carbopol surface, and weights were placed on top of the bar to add a moment, and hence load, to force the indenter to penetrate the substrate. For most of the experiments, we began by smoothing the surface of the Carbopol in the tray with a levelled scraper. The weights were then incrementally added to the bar and then moved along to the end to gradually increase the load without lifting the indenter off in between. These "loading" experiments therefore marched through a sequence of equilibrium indentations, minimizing any dependence on initial position or velocity. In a number of cases, we repeated the loading sequence after relevelling the surface, to verify the repeatability of the results.

Each time the load was raised, the depth of penetration and contact length were measured after waiting a short interval. To measure the penetration depth d, a high-resolution camera took photographs of each equilibrium position of the indenter. Markers in the field of view were tracked to determine displacements in the images, and then translated to vertical penetration distances using the known orientation and distance of the camera. A tape measure adhered to the top side of the indenter permitted a visual measurement of the length of the contact curve a along the underside. Additional photographs from the side highlighted the uplifted free surface and allowed a measurement of the profile $h(x, t)$.

The Carbopol was an aqueous suspension of Ultrez 21 with a concentration of about 0.5% by mass, neutralized with sodium hydroxide. A Herschel-Bulkley fit to the flow curve measured in a rheometer (MCR501, Anton Paar, with roughened parallel plates) gave $\tau_Y \approx 38$Pa, $n \approx 0.3$ and $K \approx 30$Pa s^n. The tray was filled to layer depths h_0 between 0.6 cm and 6.2 cm, and was lined with sandpaper to minimize any effective slip.

For the indenter, we used either a section of a cylinder (of radius $R = 7.2$ cm and width $W = 30.3$ cm), or a plate (of length $a_p = 6.8$ cm and width $W = 26.9$ cm), both made of perspex. Further experiments using a sphere are described in appendix A.

(b) Penetration depths and contact lengths

Figure 7(a,c) displays the results for the penetration depth d and contact length a. Both depend on the layer depth, and the trends with load compare poorly with a prediction of Spencer [19] for an infinitely deep layer (included as solid lines in the figure). In panels (b) and (d), the data are rescaled according to the viscoplastic lubrication theory, plotting $\delta = d/h_0$ and $a/x_0 = a/\sqrt{Rh_0}$ against $\mathcal{M}$. Although there are some discrepancies, particularly for the deeper Carbopol layers, the model broadly reproduces the experimental data. Importantly, the effect of gravity on the material beyond the contact line is significant, with the theory for $\mathcal{G} \to 0$ overestimating the penetration of the cylinder.

By contrast, the comparison of theory and experiment for the plate is less satisfactory: figure 8 shows the penetration depths and compares the resulting data for δ with the lubrication theory predictions. Although there is an abrupt increase in penetration past at a certain layer-depth-dependent load in the experiments, there is no true threshold below which the plate sits on the undeformed surface. The absence of a threshold could be due to viscoelastic deformation below the yield stress (a feature of Carbopol seen in other contexts [7,25,28]), although surface tension and its repercussions on the wetting of the plate may also contribute.

In addition, the relatively abrupt penetration of the plate occurs at higher loads than expected in the theory, for which the threshold is $\mathcal{M} = 2$. In fact, as exposed in §2(a), the threshold is underestimated in the shallow-layer model because of edge effects: slipline theory for a plate of finite length implies that $\mathcal{M} \approx 2(1 + 8.32h_0/a_p)$ (see figure 3). The revised threshold implies that the plate begins to penetrate when $\mathcal{M}$ is over the range $3.5 - 5.7$ for the experiments shown in figure 8, which is much closer to the observations.

Another potential source of disagreement arises from the way in which we conduct the loading experiments: at each load, the penetration depth was measured after ten or so seconds. Given the shallowness of the layer and the finite and fixed length of the plate, however, it is conceivable that fluid takes longer to be squeezed out from underneath. To explore this in more detail, we carried out an additional experiment in which we increased the load linearly up to 1 kg and then waited, recording the instantaneous penetration depth every ten seconds. The inset of figure 8(b) shows the results. Evidently, the plate does not reach its resting position within the ten second period after changing the load, and continues to descend by over a millimetre for about a minute after the maximum load is attained. Thus, time-dependent dynamics are at least partly responsible for the discrepancy in figure 8(b).
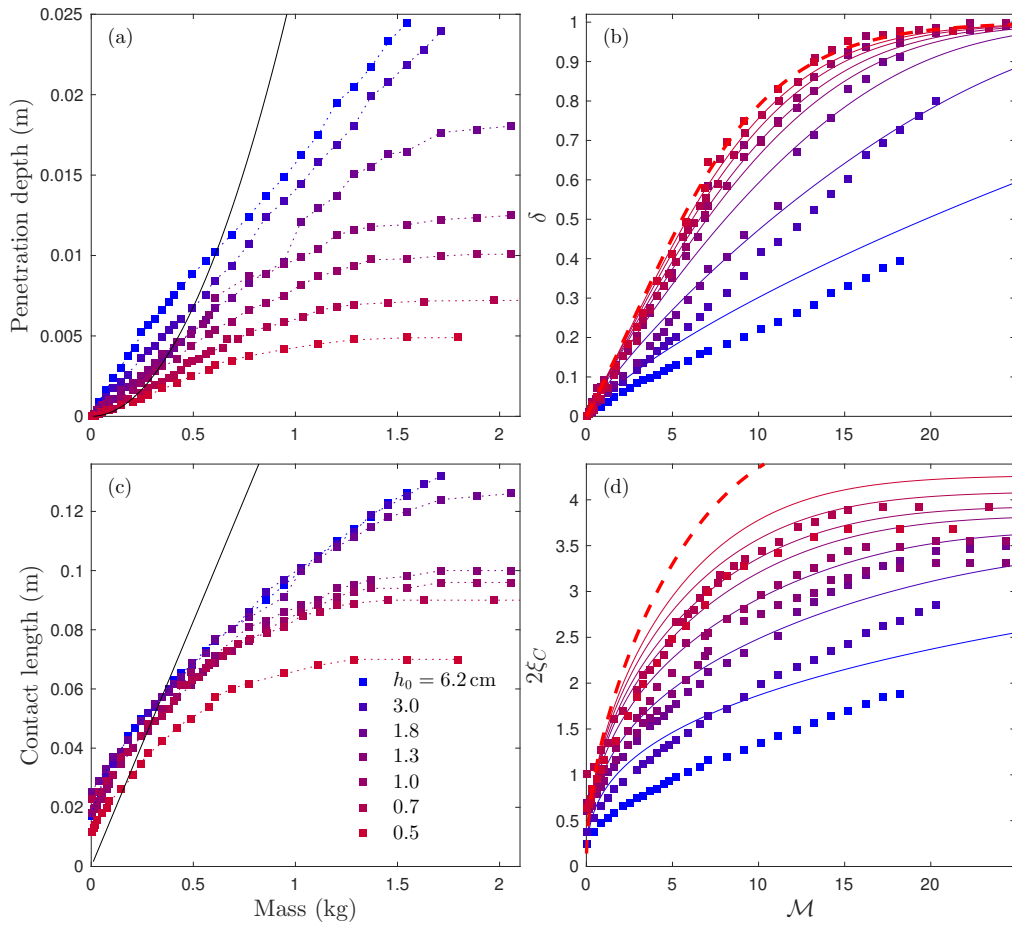
Figure 7: (a) Penetration depth d and (c) contact length a for indentations of the cylinder into Carbopol layers of different depth h_0 (as indicated by the colour scheme in (c)); solid lines show Spencer's predictions, $d = m^2 g^2 / [14R(2+\pi)^2 W^2 \tau_Y^2]$ and $a = mg/[(2+\pi)W\tau_Y]$, for a infinitely deep plastic layer. In (b) and (d), the dimensionless equilibrium position $\delta = d/h_0$ and contact length $2\xi_C = a/x_0 = a/\sqrt{h_0 R}$ are plotted against the dimensionless load $\mathcal{M} = mgh_0/(\tau_Y W x_0^2)$; the solid lines show the prediction of the shallow-layer theory of 3(f)i and the dashed line is the $\mathcal{G}/\mathcal{M} \to 0$ limit with $\delta \to 1 - 3/(2 + e^{\mathcal{M}/4})$ and $\xi_C \to \sqrt{6\delta}$.

(c) Uplifted surface profiles

Figure 9 shows sample profiles of the uplifted free surface outside the cylinder. Given a point (x_*, h_*) on the free surface to the left of the cylinder, the lubrication theory result in (3.28) predicts that the (dimensional) free surface is given by

$$h = \sqrt{h_*^2 + \tau_Y(x - x_*)/(\rho g)}, \tag{5.1}$$

whereas Spencer's [19] prediction for infinite depth is

$$h = h_* + (x^2 - x_*^2)/(14R). \tag{5.2}$$

Figure 9 compares these predictions with the experimental profiles, using the observed points indicated by circles. For the largest penetration depths, the profile steepens up close to the theoretical prediction of viscoplastic lubrication theory. However, for the smallest penetration depths, this prediction performs poorly and Spencer's result is superior, implying these
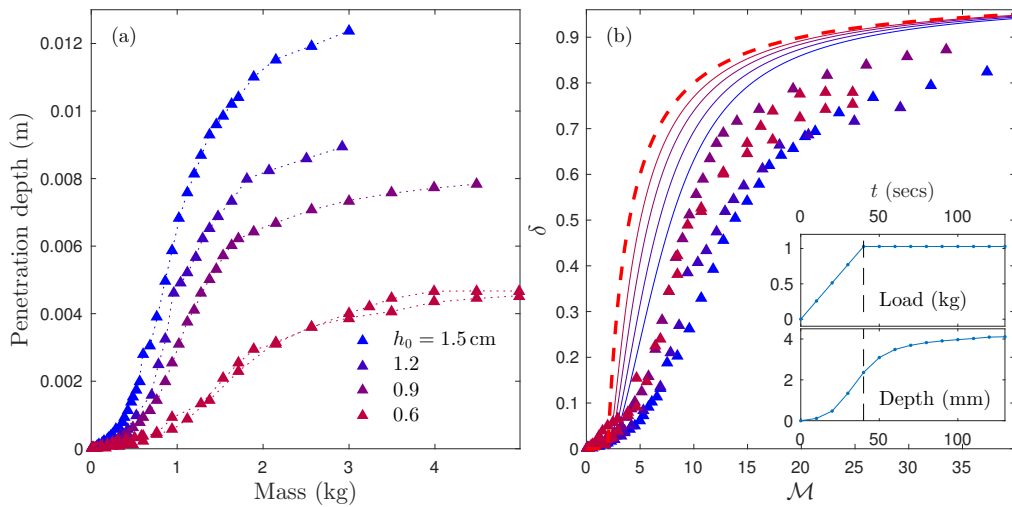
Figure 8: Indentations of the plate into Carbopol layers of different depth h_0, with penetration depths plotted as in figure 7. In (b), the dashed line with $\delta = 1 - 2/\mathcal{M}$ shows the $\mathcal{G}/\mathcal{M} \to 0$ limit. The inset plots an additional experiment where the load is increased up to $1\,\mathrm{kg}$ then held fixed.
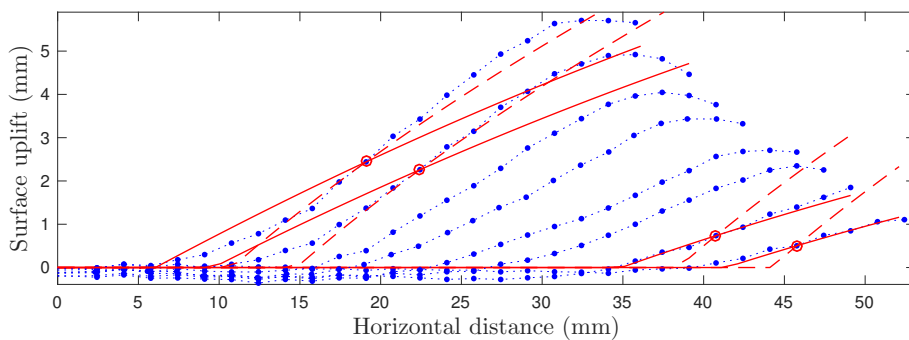

Figure 9: Profiles of the free surface deformation in Carbopol for the cylinder with $h_0 = 1.2$cm. The theoretical predictions in (5.1) and (5.2), pinned at the points indicated by the circles, are plotted as solid or dashed lines (respectively).

indentations are effectively deep. Note that the observed profiles flatten out near the cylinder and outer edges, perhaps due to the influence of surface tension and the dynamics at the contact line that reconciles the squeeze and free-surface flow patterns (see also [11]).

6. Indentation experiments with granular layers

We conducted complementary experiments for the indentation of a cylinder into a layer of glass spheres (technical quality ballotini, from Potters Industries) with diameter $D = 0.1$, 0.25, 0.5 and $1\,\mathrm{mm}$. The bulk density is $\rho \approx 1.5\,\mathrm{g/cm^3}$, and the angle of repose, as measured from building sandpiles, was about $24°$ for all four particle diameters. Once more, we measured the position of the indenter using markers in recorded images and visually measuring the contact length. In addition, however, we used a laser line incident in a vertical plane to highlight a section along the ballotini surface perpendicular to the axis of the cylinder. The deflections of the laser line occuring due to the uplift of the ballotini surface were recorded by a camera positioned off to one side at
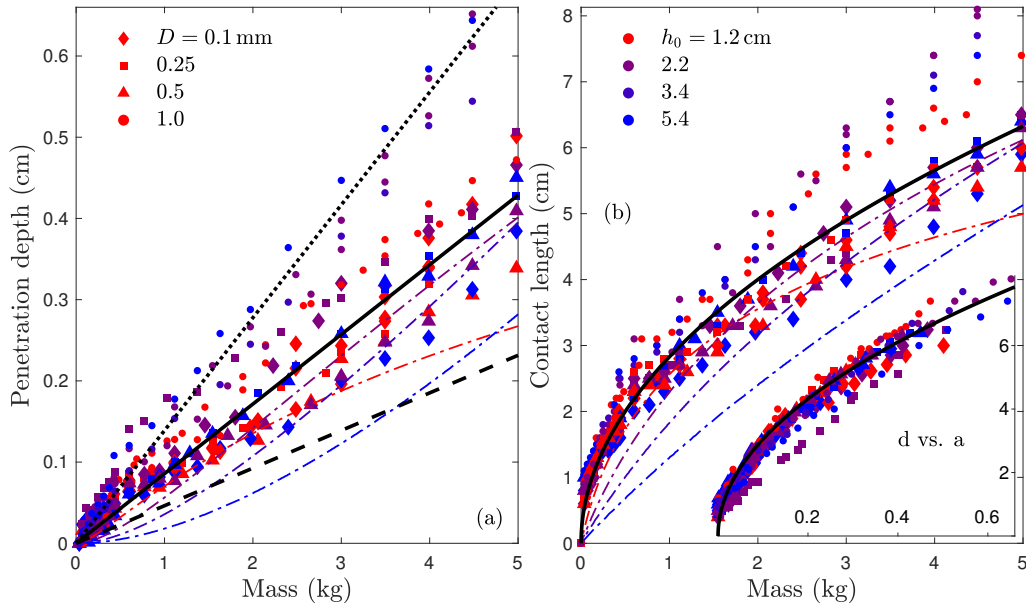
Figure 10: (a) Penetration depth d and (b) contact length a for indentations of the cylinder into ballotini. To remove an offset in the penetration depths that arises because the surface is not smooth and the counterbalancing is imperfect, the depth measurement at the lowest mass was subtracted from the data for d. The solid line plots the slipline prediction for the contact length $a = (2m/\rho N_\gamma W)^{1/2}$ along with approximation $d \approx m/(6.5R\rho N_\gamma W)$, where $N_\gamma = 5.5$. The dotted and dashed lines in (a) are the bounds, $d = m/(12R\rho N_\gamma W)$ and $d = m/(4R\rho N_\gamma W)$. The dot-dashed lines plot the shallow layer theory with $\phi = 24°$ for a fully rough cylinder and each layer depth (corresponding to $\epsilon = 0.41,\ 0.55,\ 0.69$ and 0.87). The inset in (b) plots d against a (in cm); the solid line shows the fit $a \approx 3.6\sqrt{Rd}$.

a known angle to the vertical, and the ballotini surface thereby identified. Unless the cylinder was raised from the surface after each indentation (which inevitably also disturbs the surface), a portion of the laser line is distorted by its passage through the cylinder. In our sequential loading experiments, we corrected for this distortion by subtracting off a reference profile of the counterbalanced cylinder resting just above the surface. Despite this subtraction, the indentation of the cylinder shifts the distorted section of the laser line, leaving inconsequential but unsatisfying residual optical features in the recorded signal. The penetration depth and contact length can also be extracted from the laser profiles and we verified that the two sets of measurements were in agreement.

Figure 10 shows penetration depth d and contact length a for indentations with different layer depths h_0 and particle diameters D. For the particles with $D < 1\,\text{mm}$, both d and a appear to be insensitive to particle diameter and layer depth. The $D = 1\,\text{mm}$ data are slightly different, suggesting a finite-size effect for that ballotini (such as persistent force chains spanning the layer [29]). The independence of layer depth suggests that the indentation into the granular substrate does not feel the underlying surface, which is surprising in view of the results for Carbopol and the slipline theory, in which deformation extends to the base for $a \gtrsim h_0$ (figure 3).

According to slipline theory (§2), the contact length for a deep (non-cohesive) Mohr-Coulomb layer is given by $a = (2m/\rho N_\gamma W)^{1/2}$. For a material with $\phi = 24°$, the Terzaghi coefficient is $N_\gamma \approx 5.5$ for a fully rough cylinder, and $N_\gamma \approx 3$ if the surface is perfectly smooth [30]. The contact length data in figure 10(b) is best reproduced by the slipline prediction with the Terzaghi coefficient for a rough cylinder. For the penetration depth, one requires an assumption regarding the uplifted free surface to either side of the cylinder. The penetration depth can be bounded by assuming that the

surface purely compacts without any sideways deformation (giving $a^2 = 8Rd$; dotted line) or is pushed out incompressibly to form a vertical cliff at the contact line ($a^2 = 24Rd$; dashed line). In fact, a plot of the penetration depth against the contact length (inset of figure 10(b)) suggests that $a^2 \approx 13Rd$, which leads to the prediction for d shown by the solid line in figure 10(a).

In figure 10, we also plot the contact length and penetration depth from the shallow layer theory in §4. When we assume that the free surface sits at the friction angle, this theory significantly overestimates the contact length for a given penetration depth, suggesting that avalanching of the free surface does not dictate the profile. Instead, we adopt the fit $a \approx 3.6\sqrt{Rd}$ (in place of the constraint (4.15)), which leads to the dot-dashed curves in figure 10 for a rough cylinder. The experimental trends for d and a are somewhat better captured by the deep layer theory, perhaps due to the fact that the aspect ratio ϵ is never very small. However, the shallow-layer theory also does not predict a pronounced layer-depth dependence as might have otherwise been expected. Thus, the experimental results do not necessarily imply that the deformation fails to reach the base of the layer.

Figure 11 shows surface profiles for the ballotini extracted using the laser line. The profiles show some irregularities due the optical distortions from the passage of the laser through the cylinder. However, some of the other sharp variations for the shallower layers are genuine features that emerge from abrupt uplifts of sections of the surface in the manner of sudden slip events, with the sharp features appearing to be lines of failure. For the most part, the surface profiles can be fairly satisfyingly collapsed using the scalings, $x/\sqrt{Rd}$ and $(z - h_0)/d$. This collapse allows the extraction of average, or "master", profiles that are weakly sensitive to particle diameter and layer depth for $D < 1\,\text{mm}$ and $h_0 > 1.2\,\text{cm}$ (at the shallowest layer depth ($h_0 = 1.2\,\text{cm}$), the master profiles become significantly disfigured by the slip events, which lead to distinct maxima away from the cylinder and "humped" profiles). The profiles descend almost linearly from a maximum of $(z - h_0)/d \approx 0.6$ at the side of the cylinder, down to the undisturbed surface for $x/\sqrt{Rd} \approx 5$. The contact line occurs at $x/\sqrt{Rd} \approx 1.8$, in agreement with the fit $a \approx 3.6\sqrt{Rd}$ of figure 10. In view of the scaling, the slope of the uplift depends on the depth of penetration and does not steepen to the angle of repose, ruling out surface avalanching as the origin of the profile. The master profiles can also be integrated horizontally to furnish the (signed) area of the deformed layers relative to the undeformed surface. These areas turn out to be relatively small (the integral averages of the scaled surface heights are order 10^{-2}, in comparison to the profiles themselves which ascend from -1 up to 0.6), suggesting that the penetration of the cylinder does not compact the ballotini and incompressibly uplifts the free surface.

7. Discussion

(a) Dynamic indentation

In shallow-layer theory, the final resting position of the indenter is not necessarily the equilibrium position studied in the sequential loading experiments, but below that height as a result of inertial effects. In particular, in the plastic limit ($\mathcal{V} \to 0$), and with an indenter whose mass far exceeds that of the deforming substrate ($\mathcal{G}/\mathcal{M} \to 0$), the dimensionless equation of motion of the descending object takes the form, $\ddot{\delta} = -V'(\delta)$, where $V(\delta)$ is a potential function representing the indenter's weight and substrate resistance. This equation of motion is conservative because the plastic resistance of the substrate is rate-independent, but only applies up to the point that $\dot{\delta} = 0$. Thus, given an initial speed $\dot{\delta}_0$ at the undeformed substrate surface, the final depth of penetration δ_f is given by the integral, $\frac{1}{2}\dot{\delta}_0^2 = V(\delta_f)$, if we set $V(0) = 0$. For example, with a plate or cylinder pushed into a purely cohesive layer,

$$V(\delta) = \begin{cases} -\delta - 2\mathcal{M}^{-1}\ln(1-\delta) & \text{(plate)}, \\ -\delta + 2\mathcal{M}^{-1}\left[(1+2\delta)\ln(1+2\delta) + 2(1-\delta)\ln(1-\delta)\right] & \text{(cylinder)}, \end{cases} \tag{7.1}$$
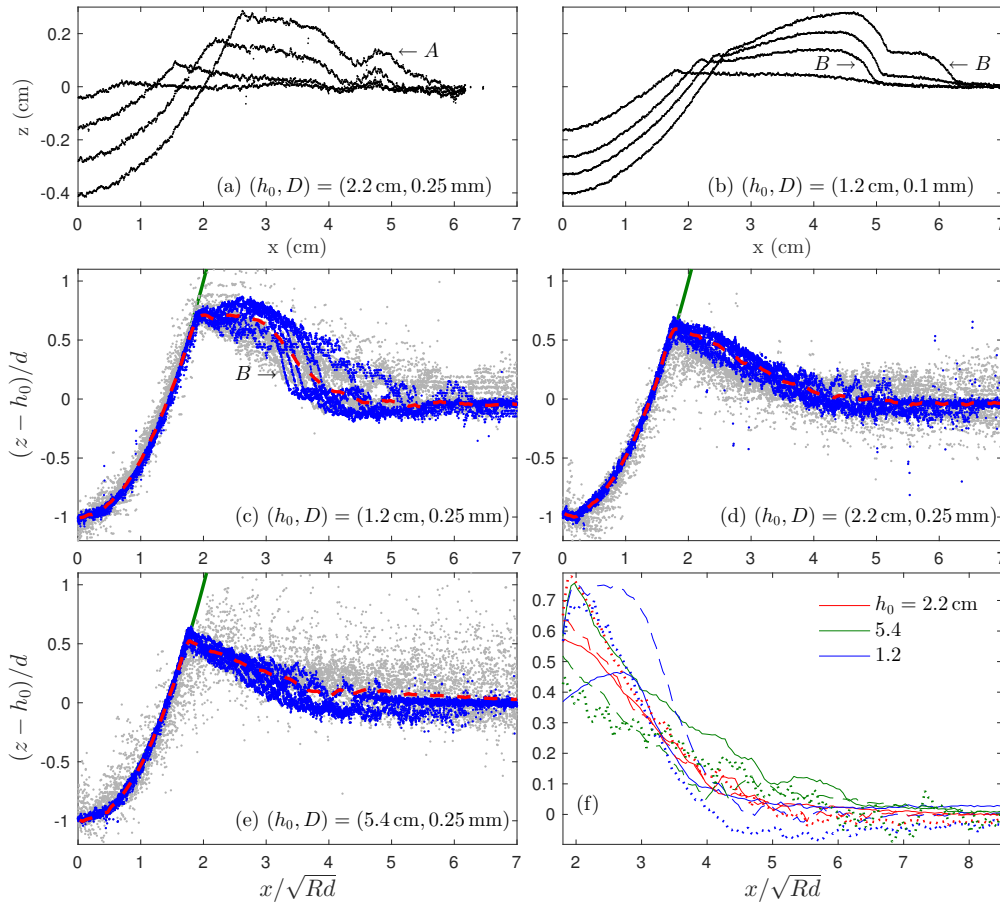
Figure 11: (a)-(b) Ballotini surface profiles for the layer depths h_0 and particle diameters D indicated. (c–e) show scaled profiles for the (h_0, D) combinations indicated, with the seven deepest penetrations in darker blue and ten shallower penetrations in light gray. The dashed lines show the averages of the data and the green solid lines indicate the cylinder. (f) plots the averaged scaled profiles, with the different layer depths colour coded as indicated and the particle diameters $D = 0.1$mm (solid), 0.25mm (dashed) and 0.5mm (dotted). Features marked A denote optical distortions through the cylinder; B denotes a genuine sharp variation in the surface.

which are illustrated in figure 12, and indicate how the final penetration depth can be determined from $\dot{\delta}_0$. If $\frac{1}{2}\dot{\delta}_0^2 > V(1)$, then $\delta_f = 1$ and the indenter is predicted to impact the underlying surface. Although this is not predicted for the plate (for which $V(\delta)$ diverges for $\delta \to 1$), δ_f can vanish for the cylinder, even though the equilibrium height is always finite.

It was possible to confirm the effect of the initial speed $\dot{\delta}_0$ on the final depth δ_f experimentally by dropping the cylinder from various heights, rather than loading it up sequentially. For example, for the 1mm ballotini, with a layer depth of $h_0 = 5$ cm, when the initial height of the cylinder was raised by tens of centimetres, the final penetration depth increased significantly from about 2mm to 6mm.

(b) Lift-off dynamics

Indentation is the first phase in the process of creating an imprint in a plastic layer; the second phase is pull-out or lift-off. For example, an idealized model for the formation of a footprint
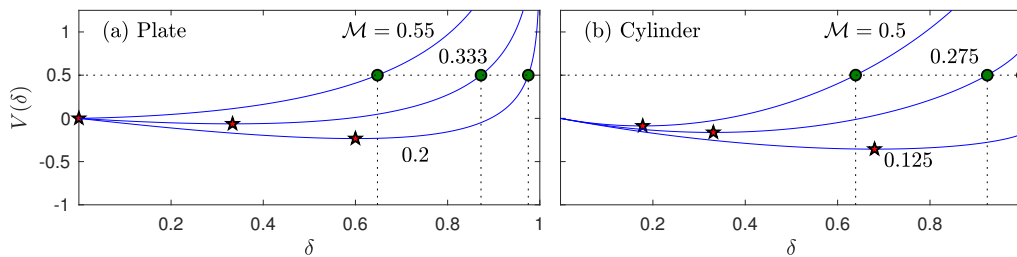
Figure 12: Potential functions $V(\delta)$ for (a) the plate and (b) the cylinder for three values of $\mathcal{M}$ indicated. The stars show δ_{eq}; the dots indicate δ_f assuming that $\dot{\delta}_0 = 1$. For the plate, $\delta_{eq} = 0$ if $\mathcal{M} < 2$ (but the plate still penetrates to $\delta_f > 0$ for $\dot{\delta}_0 > 0$) and contact canno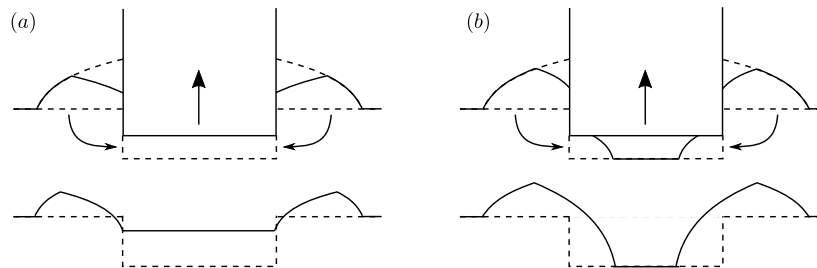t be established with the underlying surface $\delta_f < 1$. For the cylinder, contact is possible when $\frac{1}{2}\dot{\delta}_0^2 > V(1)$.

Figure 13: Lift-off mechanisms: (a) reverse squeeze flow, (b) avalanching.

combines fixed-load penetration with fixed-speed lift-off. The latter depends critically on the surface interaction between the indenter and substrate. Two obvious possibilities are illustrated for an indenting plate in figure 13: in the first, there is a partial loss of contact at the sides, with a reverse squeeze flow underneath. For the second, an immediate loss of contact occurs wherever normal forces are negative, with ensuing surface avalanching.

A reverse squeeze flow arises when no air or ambient fluid can fill the gap as the indenter is lifted up, and instead suction draws material back in from the uplifted material beyond the contact line (figure 13(a)). The free surface then collapses back towards the indenter with a profile again predicted by the free-surface flow problem. Conservation of mass ultimately determines the portion of the free surface that collapses backwards, and hence the maximum free surface height. When the free surface meets the corner the pressure at the edge of the indenter becomes atmospheric; there are then two possibilities for final lift-off. For a material with no strength under tension, the indenter detaches completely leaving an imprint. For a viscoplastic fluid like Carbopol, however, there is adhesion to the indenter surface, and detachment only occurs when the lengthening filament connecting the adhered fluid to the residual layer beneath eventually pinches off and breaks, as illustrated in figure 14. This more fluid-like phenomenon completely destroys the impression made during the indentation phase, leaving little by way of an imprint.

Immediate detachment with avalanching occurs when air or ambient fluid migrates freely into the gap underneath the lifted indenter. Only where the substrate material is pushed back into the gap is any contact maintained (figure 13(b)). Once the indenter fully detaches, the base of the imprint remains at the original penetration depth, with the collapse of the surrounding mound of material encroaching on the sides of the initial impression. Figure 15 shows two lift off experiments with ballotini at different initial depths for a cylindrical indenter. In figure 15(a), the indentation is sufficiently shallow that the sides remain below the angle of friction. As a result, almost no avalanching occurs during lift-off. However, for the deeper indentation depth in
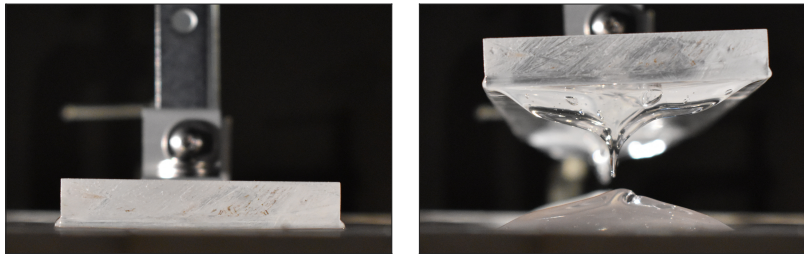
Figure 14: Photographs of lift-off experiments with Carbopol showing the effects of adhesion.
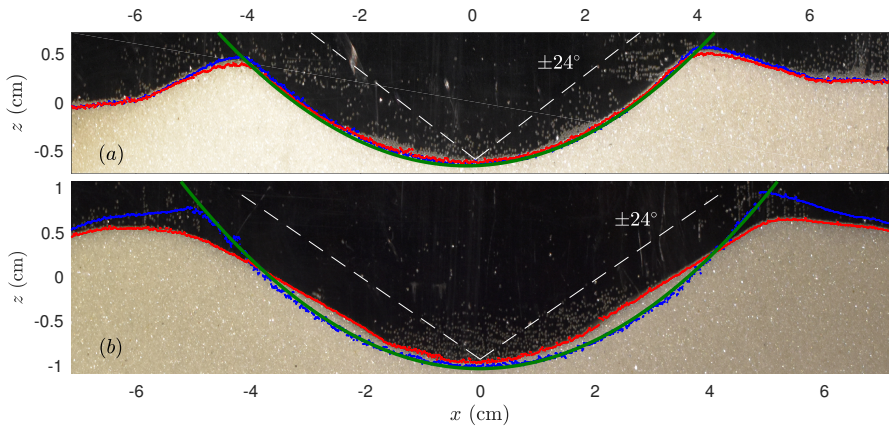

Figure 15: Profiles of the ballotini surface before (blue) and after (red) the lift-off of the cylinder. (a) Shallower indentation with minor surface motion generated by lift-off. (b) Deeper indentation, with significant inward avalanching occurring due to lift-off. $D = 0.1\,\mathrm{mm}$. The green line indicates the position of the cylinder before lift-off. The white dashed lines show the angle of friction ϕ.

figure 15(b), the walls become steeper than the angle of friction at the contact lines. In this case, ballotini avalanches down into the interior of the imprint during lift-off. The final profile then sits at an angle less than the angle of friction everywhere.

8. Conclusions

In this paper, we have explored the indentation of a planar object into a plastic layer, both theoretically and experimentally (we also provide a brief discussion of the axisymmetric indentation of a sphere in the Appendix). On the theoretical side, we outlined a viscoplastic lubrication analysis for a purely cohesive substrate that permits one to follow the finite deformations during indentation that enable the indenter to sink to its final resting position and uplift the surrounding free surface. We further provided a related analysis of dynamic indentation with arbitrary shapes into a Mohr-Coulomb layer, based on an extension of a theory by Marshall [23]. Both analyses can be used to predict the depth to which the indenter penetrates, given the load, and examine the effect of that object's inertia, which are key for modelling the formation of an imprint. The manner in which the indenter is subsequently pulled off the layer similarly impacts such prints, the phenomenology of which we have also commented upon.

For the experiments, we used layers of Carbopol and glass spheres (ballotini), which are prototypical examples of a viscoplastic fluid and a granular medium. Experiments in which a

cylinder was indented into Carbopol showed a clear dependence on the depth of the layer and compared favourably with the predictions of viscoplastic lubrication theory; the indentations with a sphere showed a similar level of agreement. Indentations with a plate were less successful, likely due to a combination of non-ideal fluid rheology, finite-depth effects, and a lengthy experimental relaxation time.

For the ballotini, indentations with a cylinder had the surprising feature that the penetration depth and contact length were insensitive to the layer depth. This is potentially unexpected in view of the Carbopol experiments and classical results from slipline theory, which suggest that deformation spans the substrate when the width of the indenter is comparable to layer depth (which was certainly the case in the experiments). The lack of a prominent layer-depth dependence is, however, anticipated by the Mohr-Coulomb shallow-layer theory; evidently, the varying contact length and layer thickness during indentation are sufficient to offset the dramatic pressure rise underneath the indenter which would otherwise characterize the confined deformation and prompt a significant dependence on layer depth.

Our success in reproducing the dynamics of indentation into a viscoplastic fluid suggests that lubrication theory offers a convenient pathway to study the formation of an imprint or the migration of structures over plastic layers. For biological inference from footprints, one can supplement the modelling of the indentation phase with a complementary analysis of the lift-off stage. In principle, this would provide a relatively simple theoretical description of the formation of the footprint, allowing one to concisely decipher the controlling combinations of physical parameters and how the imprint depends upon them. Currently, most theoretical investigations into indentations into plastic layers proceed *via* numerical computation (e.g. [11]); viscoplastic lubrication theory offers a largely analytical alternative. Despite this, the main challenge for a layer of non-cohesive material is to adequately capturing the flow dynamics outside the indenter in order to avoid an unrealistic or empirical prescription for the deformation of the free surface (which we were forced into here; see figure 10).

A. Indentation of a sphere

The analysis described in §3 can be extended to model shallow axisymmetric indentation by a sphere of radius R, for which

$$h(r,t) = h(0,t) + r^2/(2R), \tag{A 1}$$

where r is the radial coordinate. The analysis then follows that of the two-dimensional case described where the depth-integrated mass conservation (3.12) can now be written as

$$\frac{\partial h}{\partial t} + \frac{1}{r}\frac{\partial}{\partial r}\left(r\int_0^h u\,\mathrm{d}z\right) = 0. \tag{A 2}$$

The squeeze flow now occupies $r < r_c(t)$ and the substrate resistance is $2\pi\int_0^{r_c} p(r,h,t)r\,\mathrm{d}r$. Otherwise, the lubrication theory proceeds much as in the main text.
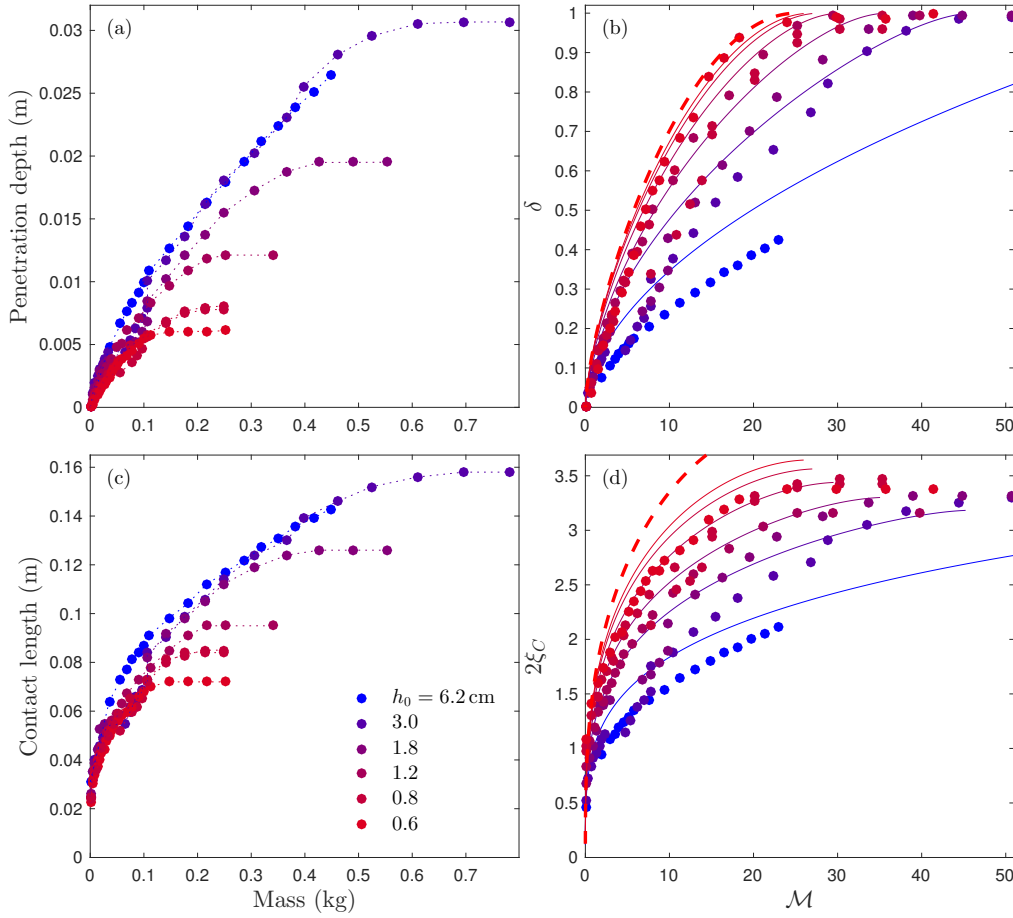
Figure 16: Indentations of the sphere into Carbopol layers of different depth h_0, with data plotted as in figure 7. In (b) and (d), the dashed line shows the $\mathcal{G}/\mathcal{M} \to 0$ limit, $\xi_C \to 2\sqrt{\delta}$ and (A 3).

In the plastic limit, $\mathcal{V} \to 0$, following the analysis in §3(f), we obtain

$$\mathcal{M} = 4\pi\left(\xi_C - \sqrt{2(1-\delta)}\tan^{-1}\frac{\xi_C}{\sqrt{2(1-\delta)}}\right) + \tfrac{1}{4}\pi\mathcal{G}\xi_C^4 \tag{A 3}$$

and

$$\delta\xi_C^2 - \tfrac{1}{4}\xi_C^4 = \frac{\mathcal{G}^2}{120}(\eta_C-1)^3(8\eta_C 2 + 9\eta_C + 3) + \frac{\xi_C\mathcal{G}}{3}(\eta_C-1)^2(2\eta_C+1), \tag{A 4}$$

where now $\xi_C = r_c/\sqrt{h_0 R}$. Again, we find the limits $\xi_C = 2\sqrt{\delta}$ for $\mathcal{G} \ll 1$ and $\eta_C \to 1$ (or $\xi_C \to \sqrt{2\delta}$) for $\mathcal{G} \gg 1$. Now, however, contact $\delta = 1$ is established when $\mathcal{M} \to 4\pi\xi_C$ with

$$\xi_C^2 - \tfrac{1}{4}\xi_C^4 = \frac{\mathcal{G}^2}{240}(\tfrac{1}{2}\xi_C^2-1)^3(4\xi_C^4+9\xi_C^2+6) + \frac{r_c\mathcal{G}}{3}(\tfrac{1}{2}\xi_C^2-1)^2(\xi_C^2+1). \tag{A 5}$$

Here, contact is an artefact of the neglect of the rate-dependent stress: for $\eta \to 0$, viscous effects become important for any finite $\mathcal{V}$ in (3.21) and the plastic limit is no longer valid.

Experiments were also conducted with a sphere, characteristic length $R = 7.4\,\mathrm{cm}$, using the setup described in §5(a). Figure 16 shows a plot of the penetration depth and contact length for the sphere. As with the cylinder described in the main text, the viscoplastic lubrication theory compares well with the experiments.

References

1. Prandtl L. 1920 Über die Härte plastischer Körper. *Nachrichten von der Gesellschaft der Wissenschaften zu Göttingen, Mathematisch-Physikalische Klasse* pp. 74–85.
2. Hill R. 1950 *The Mathematical Theory of Plasticity*. Clarendon Press, Oxford.
3. Terzaghi K. 1943 *Theoretical Soil Mechanics*. John Wiley & Sons, New York.
4. Marshall EA. 1968 Rolling contact with Plastic Deformation. *J. Mech. Phys. Solids.* **16**, 243–254.
5. Collins IF. 1972 A Simplified Analysis of the Rolling of a Cylinder on a Rigid/Perfectly Plastic Half-Space. *Int. J. Mech. Sci.* **14**, 1–14.
6. Hill R, Storakers B, Zdunek AB. 1989 A Theoretical Study of the Brinell Hardness Test. *Proc. R. Soc. A* **423**, 301–330.
7. Maillard M, Mézière C, Moucheront P, Courrier C, Coussot P. 2016 Blade-coating of yield stress fluids. *J. Non-Newtonian Fluid Mech.* **237**, 16–25.
8. Engmann J, Servais C, Burbidge AS. 2005 Squeeze flow theory and applications to rheometry: a review. *J. Non-Newtonian Fluid Mech.* **132**, 1–27.
9. Mitsoulis E. 2007 Flows of viscoplastic materials: models and computations. *Rheology Reviews* pp. 135–178.
10. Hewitt IJ, Balmforth NJ, McElwaine JN. 2012 Granular and fluid washboards. *J. Fluid Mech.* **692**, 446–463.
11. Merifield RS, White DJ, Randolph MF. 2009 Effect of surface heave on response of partially embedded pipelines on clay. *J. Geotech. Geoenviron.* **135**, 819–829.
12. White DJ, Randolph MF. 2007 Seabed characterisation and models for pipeline-soil interaction. *Int. J. Offshore Polar* **17**.
13. Allen JRL. 1997 Subfossil mammalian tracks (Flandrian) in the Severn Estuary, S. W. Britain: mechanics of formation, preservation and distribution. *Philos. Trans. R. Soc. B Biol. Sci.* **352**, 481–518.
14. Bates KT, Savage R, Pataky TC, Morse SA, Webster E, Falkingham PL, Ren L, Qian Z, Collins D, Bennett MR, McClymont J, Crompton RH. 2013 Does footprint depth correlate with foot motion and pressure?. *J. R. Soc. Interface* **10**.
15. Milan J. 2006 Variations in the Morphology of Emu (Dromaius Novaehollandiae) Tracks Reflecting Differences in Walking Pattern and Substrate Consistency: Ichnotaxonomic Implications. *Palaeontology* **49**, 405–420.
16. Salençon J. 1977 *Application of the theory of plasticity in soil mechanics.* John Wiley & Sons.
17. Mandel J, Salençon J. 1972 Force portante d'un sol sur une assise rigide. *Geotechnique* **22**, 79–93.
18. Spencer AJM. 1960 Pertubation Methods in Plasticity - I Plane Strain of Non-Homogeneous Plastic Solids. *J. Mech. Phys. Solids* **9**, 279–288.
19. Spencer AJM. 1962 Pertubation Methods in Plasticity - II Plane Strain of Slightly Irregular Bodies. *J. Mech. Phys. Solids* **10**, 17–26.
20. Hewitt IJ, Balmforth NJ. 2012 Viscoplastic lubrication theory with application to bearings and the washboard instability of a planing plate. *J. Non-Newtonian Fluid Mech.* **169**, 74–90.
21. Balmforth NJ, Craster RV, Rust AC, Sassi R. 2007 Viscoplastic flow over an inclined surface. *J. Non-Newtonian Fluid Mech.* **142**, 219–243.
22. Balmforth NJ. 2019 Viscoplastic Asymptotics and Other Analytical Methods. In *Lectures on Visco-Plastic Fluid Mechanics* , pp. 41–82. Springer.
23. Marshall E. 1967 The compression of a slab of ideal soil between rough plates. *Acta Mechanica* **3**, 82–92.
24. Prandtl L. 1923 Anwendungsbeispiele zu einem Henckyschen Sakz uber das plasfische Gleichgewichf. *ZAMM* **3**, 401–406.
25. Balmforth NJ, Frigaard I, Ovarlez G. 2014 Yielding to stress: Recent developments in viscoplastic fluid mechanics. *Ann. Rev. Fluid Mech.* **46**, 121–146.
26. Salençon J. 2002 The influence of confinement on the bearing capacity of strip footings. *Comptes Rendus Mécanique* **330**, 319–326.
27. Nedderman RM. 2005 *Statics and kinematics of granular materials*. Cambridge University Press.
28. Putz A, Burghelea T, Frigaard I, Martinez D. 2008 Settling of an isolated spherical particle in a yield stress shear thinning fluid. *Phys. Fluids* **20**, 033102.
29. Geng J, Howell D, Longhi E, Behringer R, Reydellet G, Vanel L, Clément E, Luding S. 2001 Footprints in sand: the response of a granular material to local perturbations. *Phys. Rev. Lett.* **87**, 035506.
30. Martin C. 2005 Exact bearing capacity calculations using the method of characteristics. *Proc. IACMAG. Turin* pp. 441–450.